Polymer Degradation and Stability 93 (2008) 1422–1432

Contents lists available at ScienceDirect

Polymer Degradation and Stability

journal homepage: www.elsevier.com/locate/polydegstab

Effect of cyclic loading on tensile properties of PC and PC/ABS

Qin-Zhi Fang [a,b,*], T.J. Wang [a], H.G. Beom [b], H.M. Li [a]

[a] MOE Key Laboratory for the Strength and Vibration of Mechanical Structures, Xi'an Jiaotong University, Xi'an 710049, China
[b] Department of Mechanical Engineering, Inha University, Incheon 420-751, Republic of Korea

ARTICLE INFO

Article history:
Received 6 April 2008
Accepted 26 May 2008
Available online 3 June 2008

Keywords:
Tensile test
True stress–strain
Cyclic loading
Large deformation

ABSTRACT

The effects of cyclic loading on tensile fracture properties of polycarbonate (PC) and the alloy of polycarbonate and acrylonitrile–butadiene–styrene (PC/ABS) are experimentally investigated in the paper. Two digital cameras are used to record simultaneously the tensile deformation of specimens and the large deformation and the necking process of these polymers are discussed. Two lateral contractions are not identical at the later tensile stages and the contraction ratios in each lateral direction are related with the tensile strains in axial direction on width and thickness surface. The curvature radiuses at the minimum section during necking process are shown. The volume increases during necking process and then decreases gradually. The yield stress and fracture stress of PC/ABS are lower than that of PC. The degradation of the fracture stress and fracture strain due to the application of cyclic loading is larger for PC than that for PC/ABS, and these can be used to explain qualitatively why PC has higher fatigue crack growth rate than PC/ABS.

© 2008 Elsevier Ltd. All rights reserved.

1. Introduction

Crazes are often generated around fatigue crack tips, which make it difficult to the measurement of the crack length as well as to the understanding of the fracture mechanism of fatigue cracks [1,2]. The deformation of craze zones at crack tips is within postyield tension stage. The cyclic deformations of the craze zones induce the fracture of the material at crack tips. Although there is some difference between the concentricity of stresses at crack tips and tensile specimens, it is expected that the tensile behaviors can be used to explain the fracture behaviors at crack tips, if the triaxiality of stresses is considered. With this consideration, O'Connel et al. [3] investigated the correlation of creep tension properties and slow crack growth. Bai and Wang [4] studied the effect of postyield cyclic loading on the plastic damage mechanisms of polypropylene/polyamide 6/polyethelene–octene (PP/PA6/POE). Besides, Li et al. [5] studied the effect of previous fatigue loading on the mechanical properties of amorphous polycarbonate, and found that the cyclic loading led to overall embrittlement of polycarbonate. Under fatigue loading condition, it seems possible to simulate the fatigue crack propagation mechanisms with the postyield cyclic loading deformation behaviors. Therefore, studies on tension and cyclic tension behaviors of polymer materials can help us to explain fatigue crack propagation properties of polymers.

On the other hand, tensile true stress–strain behavior is the most fundamental mechanical property of polymer materials and provides useful information about the yielding behavior, true strain–hardening rate, and stress-induced transformations of crystalline texture. Several papers investigated the effects of triaxial stress state on the fatigue and fracture properties of PC/ABS [6,7]. The method to obtain reliable true stress–strain relation for polymers is important in the development of constitutive models [8,9].

During uniaxial tension tests, most engineering polymers deform (with necking) inhomogeneously at relatively small strains [10,11]. Once necking occurs, traditional extensometers are virtually useless. Contact extensometers measure only the average strain over gage length. There have been numerous attempts to characterize the large-strain tensile behavior of polymers. The most successful endeavors used some type of video system to capture images of specimens at various extension stages. Buisson and Ravi-Chandar [10] painted finely spaced grid lines on the surface of rectangular bar-type PC specimens, and calculated the axial and transverse displacement gradient at points along specimen centerline by fitting polynomials to the displacement of the grid lines. G'Sell et al. [11] calculated the true stress–strain behavior of several polymers by using an optical diametral transducer to measure instantaneous minimum diameter of hourglass-shaped cylindrical specimens. Nazarenko et al. [12] used a similar technique on round polycarbonate bars but applied fine grids to specimen surface and measured the behavior at points away from the site of neck initiation. He discussed the relationship of tensile properties and the

* Corresponding author. MOE Key Laboratory for the Strength and Vibration of Mechanical Structures, Xi'an Jiaotong University, Xi'an 710049, China. Tel./fax: +86 29 82665168.
E-mail address: fangqz@mail.xjtu.edu.cn (Q.-Z. Fang).

0141-3910/$ – see front matter © 2008 Elsevier Ltd. All rights reserved.
doi:10.1016/j.polymdegradstab.2008.05.022

necking profiles. Meyer and Pruitt [13] studied the effect of cyclic true strain on the morphology, structure, and relaxation behavior of ultra-high molecular weight polyethylene with a method of measuring the distance between two grid lines spaced about 2.5 mm along the axial direction. Kurtz et al. [14] used a similar method to study yielding, plastic flow, and fracture behavior of ultra-high molecular weight polyethylene. Haynes and Coates [15] measured axial strain as a function of axial position in polypropylene and styrene butadiene elastomer by tracking the axial position of transverse grid lines printed on the surface of rectangular bar-type specimens. Gloaguen and Lefebvre [16] calculated the true stress–strain and volumetric strain behavior of nylon and polypropylene by measuring the separation of ink marks on rectangular bar-type specimens. In his work, homogeneous deformation between the ink marks was assumed. G'Sell et al. [17] developed an optical technique used on rectangular bar-type specimens, in which, seven dots on specimen surface were used to calculate the true axial and transverse strains at a particular axial location. By assuming a transversely isotropic strain tensor, they calculated the true stress–strain and volumetric strain behavior of polyethylene terephthalate and high-impact polystyrene. Laraba-Abbes et al. [18] used a digital image correlation (DIC) method to measure the nominal stress–stretch behavior of carbon black-filled natural rubber. They calculated the in-plane axial and transverse stretches by differentiating linear functions obtained by fitting to the displacement field over subsets. Instead of using laser speckle, Parsons et al. [19] used fine random artificial ink points airbrushed on specimen surfaces as digital signature of surfaces, to investigate the large-strain tensile behavior of neat and rubber-toughened polycarbonate. Fang et al. [20] studied the large deformation behavior of the alloy of polycarbonate and acrylonitrile–butadiene–styrene (PC/ABS) with DIC method by recording the deformation of two surfaces simultaneously.

In this paper, the true stress–strain behaviors of PC and PC/ABS are studied with DIC method. Without the incompressible assumption of the materials, three directional deformations are recorded simultaneously with the optical image analysis technique. Inhomogeneous deformations in two transverse directions are considered. The dilatational deformation and the necking profiles are discussed. With this method, the effects of cyclic loading on the fracture stress and fracture strain of polymer PC and PC/ABS are investigated.

2. Experimental

2.1. Materials and specimen

The polymer materials used in this study are polycarbonate (PC) and PC/ABS supplied by Nanjing Julong Engineering Plastics Corporation. The average molecular weight of PC is 30,000 g/mol. The PC material is molded to the dumb-bell tension specimen by injection with a dimension shown in Fig. 1. The injection temperature is 300–320°C. The holding pressure is around 60–80 MPa.

The minor phase ABS with pellet sizes of 0.2–0.5 μm uniformly distributes among the continuum phase PC in PC/ABS. SWA compatibilizer is added to the blend of PC and ABS before injection. The composition of the blend is 66/30/4 PC/ABS/SWA. The blend is molded into the dumb-bell tension specimen with a dimension shown in Fig. 1. The injection temperature is 240–250 °C. The holding pressure is around 60–80 MPa. The tensile specimen gage section dimensions are 70 mm × 10 mm × 4 mm.

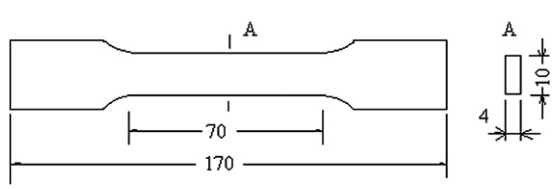

Fig. 1. Schematic depiction of the specimen.

2.2. Test configuration

All tensile tests are performed on an MTS 858 hydroelectric testing machine. Digital image correlation analysis (DIC) method is used to measure the deformations of tensile specimens. Fig. 2 shows a picture of the test set-up. To give a better characterization of the specimen surfaces, a random speckle pattern with three different colors (black, blue and red) is applied to each specimen with airbrushes filled with color ink. It is not assumed that specimens deform isotropically in the two lateral directions. Therefore, two cameras with high resolutions (3264 pixels × 2448 pixels and 2776 pixels × 2074 pixels, respectively) are used to record the deformations in width and thickness directions at regular intervals of about 30 s.

2.3. Testing procedure

All tensile tests are conducted by following ASTM D-638 standard test method at room temperature (about 15 °C). The crosshead speed is 1 mm/min during tensile loading process. To keep the photographs synchronization with the load data acquired by the test machine, efforts are made to insure the loading and two cameras starting simultaneously. Besides, the load data can also be corresponded to each photograph according to the load *vs.* time data and photo *vs.* time data. So that the load data and the photograph data can be correlated each other with a reasonable precision. To locate the necking in the gage region, the thickness near the center of the specimen is reduced by about 0.1 mm with fine sand paper. It is proved to be an effective measure to locate the necking region and has no effect on successive deformations after necking.

To study the cycling load effects on the tension fracture behavior of the polymers, a serial of tension–tension loading cycles (1, 3, 5 and 15 cycles) are applied to some specimens during tensile loading. These specimens are first loaded with a crosshead speed of 1 mm/min for 8 min, and then tension–tension loading cycles are applied. In each loading cycle, the specimens are unloaded with load control from higher load level to 100 N within 0.5 min, and then reloaded with a crosshead speed of 1 mm/min for 1.5 min. After then, the specimens are loaded with a crosshead speed of 1 mm/min to failure. As an illustration of the loading policy, a loading curve with 15 loading cycles is shown in Fig. 3.

2.4. Displacement measurement

DIC method similar to [20] is used in this study. For example, Fig. 4 shows two of the images obtained during testing. The

Fig. 2. The test set-up of the displacement measurement system.

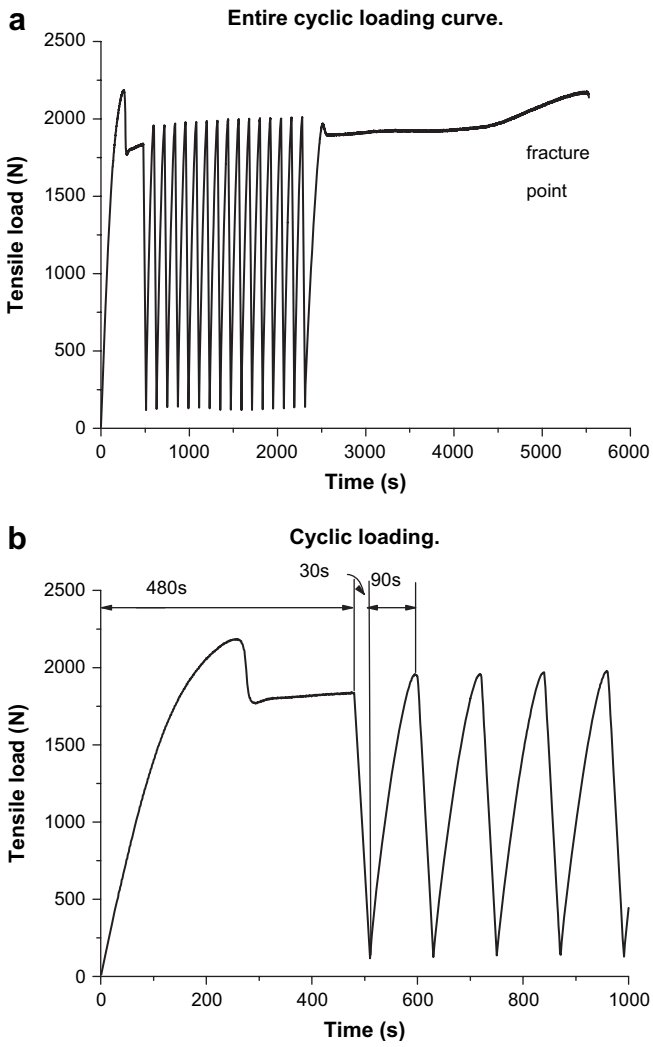

Fig. 3. Cyclic loading curve.

undeformed image is taken as reference image, and the other is taken as deformed image. An interested area and coordinates are chosen on the undeformed image. In all of the calculations, as shown in the reference image, take the axial (tension) direction as x direction, and take the lateral direction as y direction. To give the displacement (u_i, v_i) of the deformed image at point i (x_i, y_i) on the reference image, subsets with dimension of $(2n+1)$ pixel $\times$ $(2n+1)$ pixel ($x_i - n \le x \le x_i + n$ and $y_i - n \le y \le y_i + n$) is selected around point i (x_i, y_i) in the interested area. The discrete matrix of the pixel color (RGB) values in the subset forms a unique pattern within the image. The DIC method is employed to find the corresponding subset on the deformed image with image correlation technique. The detail of the method can be found in literature [20].

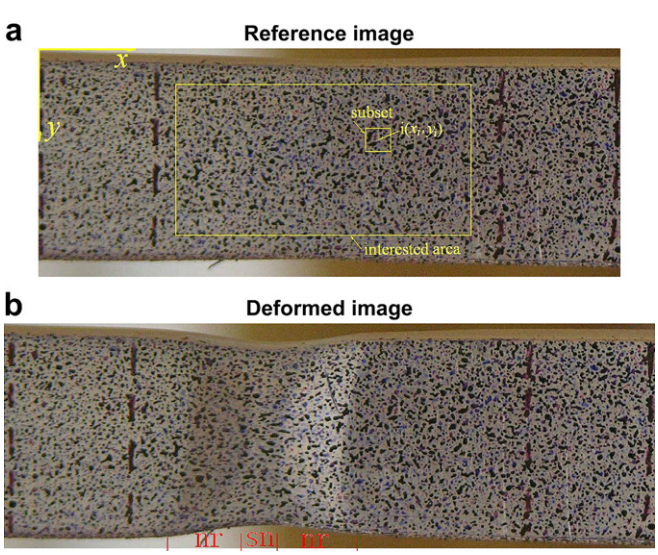

Fig. 4. Deformed and reference images. nr – necking region, sn – stable neck region.

3. Results and discussion

3.1. Displacement fields

The two images in Fig. 4 correspond to two different tensile stages. It is found that necking takes place at relative small strains. Then the necking regions (registered as that shown in Fig. 4(b)) extend along the axial (also the tensile) direction of the specimen. Normally, the necking regions (nr) will extend to the shoulders of the tensile specimen, then the specimen breaks after a little rising of the tensile load. But some specimens may break before the necking regions extended to the shoulders. By using the DIC method, the displacement fields for each image collected at different stages are given. Then the strain fields at each stage can be obtained. The accuracy of the method was presented in [20].

Fig. 5(a) shows the axial displacement fields $u(x, y)$ of a PC/ABS specimen at time = 330 s. Fig. 5(b) shows the lateral displacement fields $v(x, y)$ in the width direction of the specimen at same time. (x, y) denotes the pixel coordinates of the point in the undeformed image of the specimen. The unit of the displacement u and v is also pixel. It is found that u and v change greatly in necking regions. It is found that the shearing deformation in the necking region is nearly symmetric, no significant shear band is found in the middle of the necking region for PC/ABS. All of the displacement fields could be obtained with this method for PC/ABS and PC.

3.2. Strain fields

The normal strain and shear strain fields can be obtained from the displacement fields. For example, as shown in Fig. 5 (a), to calculate the strains at point (x_j, y_j) in xy plane, a subset such as ABCD around this point is chosen. The corresponding collections of x and y are $x_j - k_s \le x \le x_j + k_s$ and $y_j - l_s \le y \le y_j + l_s$, respectively. The integers k_s and l_s correspond to the size of subset ABCD, which are selected according the shape of the displacement fields. The displacement fields are best fitted with plane or curved functions $u(x, y)$ and $v(x, y)$ of the surface *abcd* with least-squares best-fitting method over the subset ABCD. The engineering strains are obtained from the partial derivatives $\partial u/\partial x$, $\partial v/\partial y$, $\partial u/\partial y$, and $\partial v/\partial x$ at point (x_j, y_j) in each corresponding subset.

The engineering strains are as follows:

$$\varepsilon_{ex} = \partial u/\partial x$$

$$\varepsilon_{ey} = \partial v/\partial y \qquad (1)$$

$$\gamma_{xy} = \partial u/\partial y + \partial v/\partial x$$

where ε_{ex}, ε_{ey}, and γ_{xy} are the engineering axial, lateral and shear strains, respectively. Generally, the subset size needed is smaller for more variational displacement fields than that for less variational ones. Proper subset sizes are selected in the calculation of the strain fields at each stage. Fig. 6 shows the engineering strain fields for the displacement fields in Fig. 5.

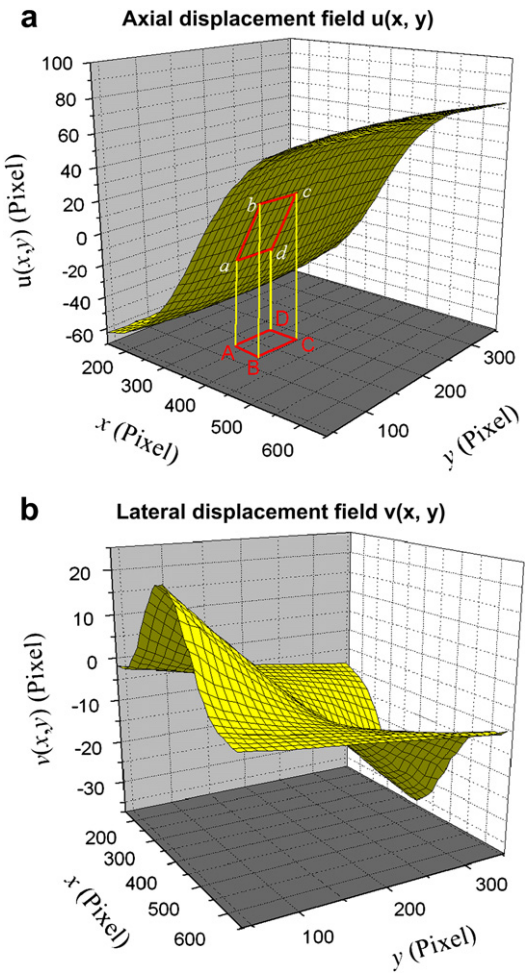

Fig. 5. The displacement fields for axial $u(x, y)$ and lateral $v(x, y)$ for a PC/ABS specimen at time = 330 s.

It has been deducted that the engineering principal strains ε_{e1} and ε_{e2} can be calculated with the strain fields obtained above by the following formula for small as well as large strains:

$$\varepsilon_{e1} = (\varepsilon_{ex} + \varepsilon_{ey})/2 + \sqrt{(\varepsilon_{ex} - \varepsilon_{ey})^2 + \gamma_{xy}^2}/2 \quad (2)$$

$$\varepsilon_{e2} = (\varepsilon_{ex} + \varepsilon_{ey})/2 - \sqrt{(\varepsilon_{ex} - \varepsilon_{ey})^2 + \gamma_{xy}^2}/2.$$

The true strains (or Hencky strain) ε_1 and ε_2 can be determined with following formula as that given in [17,19,20]:

$$\varepsilon_1 = \ln(1 + \varepsilon_{e1}) \quad (3)$$

$$\varepsilon_2 = \ln(1 + \varepsilon_{e2}).$$

It can be proved that Eq. (3) is exactly correct for principal stresses if no shear deformation occurred. This is true in the minimum section of the specimens in this study. It can be found latter in this section the shear strains are relatively small in the tensile tests. Therefore, Eq. (3) can be used approximately for all of the strain fields.

The direction of principal strain is represented with the angle to the x-axis α, which can be given with the following formula:

$$\tan 2\alpha = -\gamma_{xy}/(\varepsilon_x - \varepsilon_y). \quad (4)$$

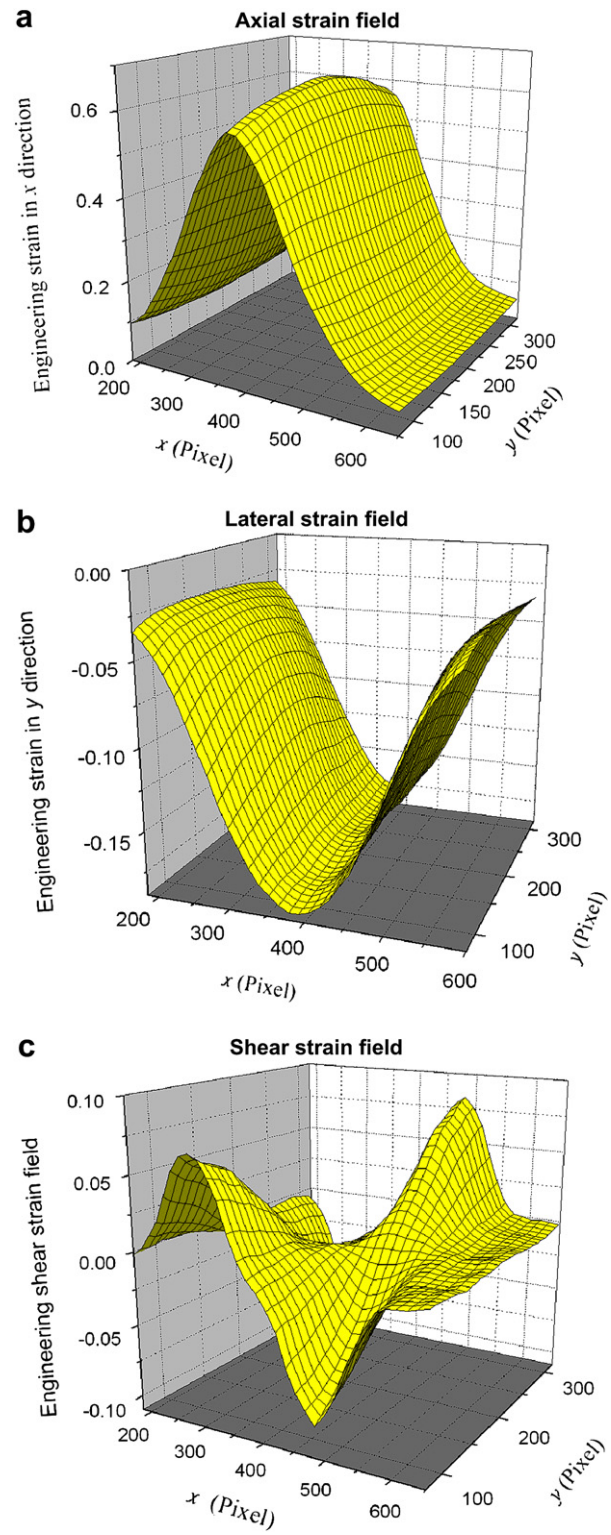

Fig. 6. The engineering strain fields for the displacement fields given in Fig. 5.

Fig. 7 shows the principal strain fields corresponding to the strain fields given in Fig. 6. It is found that the principal engineering strain fields ε_{e1} and ε_{e2} are similar with the engineering strain fields for ε_{ex} and ε_{ey}, respectively, because the shear strains are relatively small in this region. This is especially true for the strains near the middle section of the necking region. In the middle of the necking region (minimum section), the shear strains tend to be zero as shown in Fig. 6(c). Therefore, the strain fields of ε_{ex} and ε_{ey} are

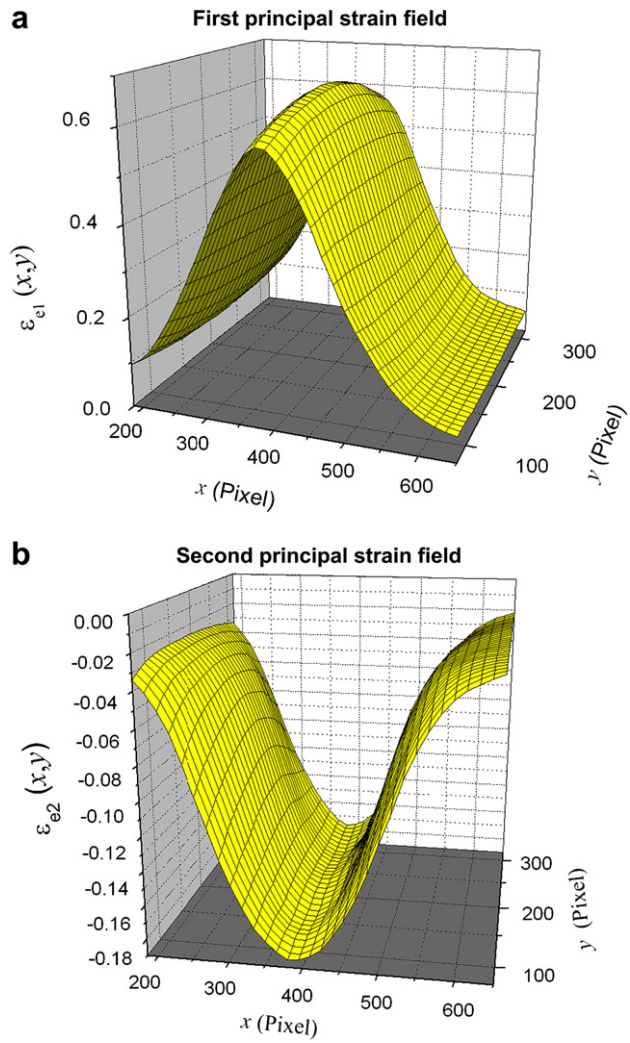

Fig. 7. The engineering principal strain fields for the displacement fields given in Fig. 5.

almost same as the principal strain fields of ε_{e1} and ε_{e2} at minimum section.

At each tension stage, the average of the tensile engineering strains ε_{ex} along the lateral (y) direction is calculated at each fixed x positions. The mean strains $\varepsilon_{etx}(x)$ and $\varepsilon_{ewx}(x)$ vary along the axial (x) direction, which are obtained from the strain fields of thickness surface and width surface, respectively. The maximum axial mean strain obtained from the thickness surface is registered as ε_{et}. The corresponding maximum tensile ratio is taken as $\lambda_t = 1 + \varepsilon_{et}$. The maximum axial mean strain obtained from the width surface is taken as the representative tensile strain of the specimen at the minimum section, and is registered as ε_e. The corresponding maximum tensile ratio is taken as $\lambda_w = 1 + \varepsilon_e$.

The average of lateral (y) strains ε_{ey} along the lateral (y) direction is calculated at each fixed x positions too. The mean strains $\varepsilon_{ety}(x)$ and $\varepsilon_{ewy}(x)$ vary along the axial (x) position are obtained from the strain fields of thickness surface and width surface, respectively. The contraction ratios along the axial (x) position $\lambda_{ety}(x)$ and $\lambda_{ewy}(x)$ are taken as $(1 + \varepsilon_{ety}(x))$ and $(1 + \varepsilon_{ewy}(x))$ for the thickness direction and width direction, respectively. The minimum of the lateral mean strains ($\varepsilon_{ety}(x)$ or $\varepsilon_{ewy}(x)$) of the specimen in each corresponding direction is registered as ε_{ewym} or ε_{etym} for the width or the thickness direction, respectively.

Therefore, the maximum contraction in width direction (i.e., the minimum value of w/w_0) is given as

$$w/w_0 = 1 + \varepsilon_{ewym}. \tag{5}$$

The maximum contraction in thickness direction (i.e., the minimum value of t/t_0) is given as

$$t/t_0 = 1 + \varepsilon_{etym}. \tag{6}$$

The true average tensile strain at the minimum section is given as

$$e_{tr} = \ln(1 + \varepsilon_e) \tag{7}$$

where w or t and w_0 or t_0 are the minimum temporary width or thickness and initial width or thickness of the specimens, respectively, and the subscript w represents data obtained from the image of width surface, and the subscript t represents data obtained from the image of thickness surface.

3.3. Necking deformation

According to [20], the lateral contraction does not deform homogeneously in two lateral directions. To give a reasonable discussion on this problem, Fig. 8(a) and (b) shows the lateral contraction ratio variation with the tensile engineering strains

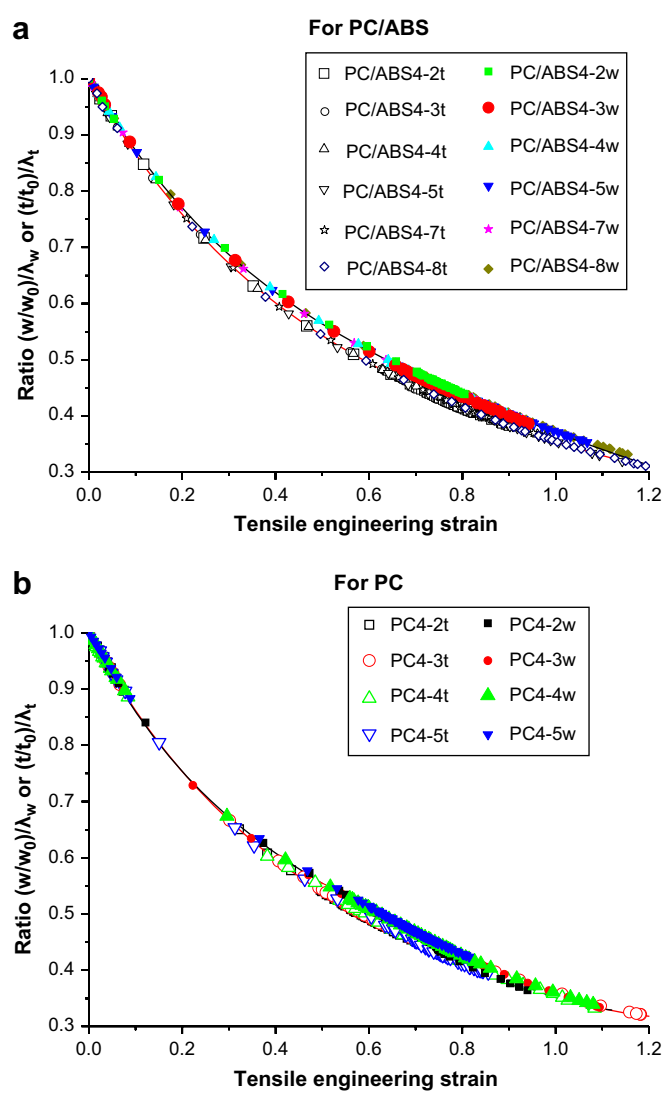

Fig. 8. Lateral contraction ratio. Here PC4-x and PC/ABS4-x are the name of specimens for PC and PC/ABS, respectively; t or w represents the thickness or width direction, respectively.

obtained with different specimens for PC/ABS and PC, respectively. It is seen from these figures that the lateral contraction ratios in width direction or in thickness direction each follow the same trend for different specimens with the same material, and can be fitted with same formulas. But there are significant differences between the contraction ratios obtained from two lateral directions. The lateral contraction in thickness direction is a little more than that in the width direction at the same tensile strain. The difference is larger for PC/ABS than that for PC. That means the contraction ratios are different for different materials. It can also be found from Fig. 8 that the differences of the contraction ratio in the two lateral directions are larger in the range of tensile engineering strains from 0.4 to 0.85 (which correspond to a range of true strains from 0.33 to 0.6) for PC/ABS (Fig. 9(a)) and PC (Fig. 9(b)).

It is easily seen from Figs. 6(b) and 7(b) that the lateral contraction strains are higher near the edges than that in the center part at the minimum section of the specimen. This means the different constraint between the two lateral directions (width and thickness) is one of the main reasons to cause the differences. The contraction ratios are geometry dependent.

Necking deformation profiles of polymers have been used to study constitutive relations decades ago [21]. With the DIC method used in this study, the development of necking profiles can be obtained.

As an example, Fig. 9(a) shows the typical half width contraction ratios ($\lambda_{ewy}/2 = (w_x/w_{0x})/2$) along the axial position of specimen PC/ABS4-2 for polymer PC/ABS. Fig. 9 (b–e) shows the specimen necking profiles at different stages which correspond to four of the curves of contraction ratio with the axial position shown in Fig. 9(a). It is noted that the curvature radius of the necking profiles at the minimum section of the specimen change with the tensile strains. The curvature radiuses can be directly measured from the pictures of the specimen at different tensile stages, such as the pictures shown in Fig. 9(b–e). In the study, they are obtained with the contraction ratio curves as shown in Fig. 9(a) by some mathematical calculation. It should be noted that the coordinates x are fixed on the undeformed image as shown in Fig. 4(a). To obtain the curvatures of the deformed necking profiles, a translation of the coordinates to the deformed specimen is made. The necking profile of width surface is given as follows:

$$X(x) = \int_{x_0}^{x} (1 + \varepsilon_{ewx}(\eta))\mathrm{d}\eta \tag{8}$$

$$Y(x) = w_0 \lambda_{ewy}(x)/2$$

here $(X(x), Y(x))$ defines the necking profile at certain tensile stage.

It is known the curvature radius r for a curve can be obtained with

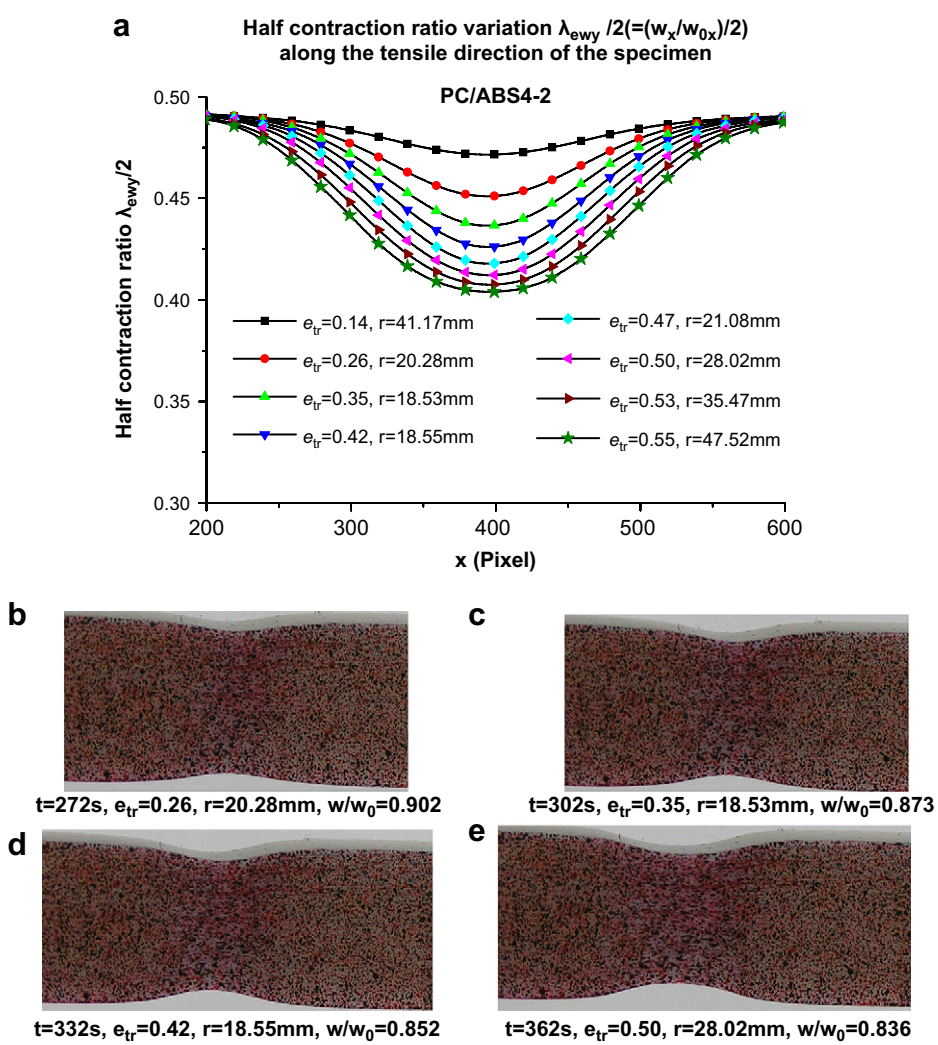

Fig. 9. Necking process and corresponding curvature radius at the minimum sections for specimen PC/ABS4-2. Here, t is the time of loading; e_{tr} and r the true strain and the curvature radius, respectively, at the minimum sections. w_x/w_{0x} is the ratio of temporary width to the initial width at the same x position. w/w_0 is the minimum section contraction ratio of the specimen in the width direction.

$$r = \frac{\left[1 + \left(\frac{dY}{dX}\right)^2\right]^{3/2}}{\left|\frac{d^2Y}{dX^2}\right|}. \tag{9}$$

Because of the derivative $\frac{dY}{dX} = 0$ at the minimum necking sections, the curvature radius of the necking profiles at the minimum section is rewritten as

$$r = \frac{1}{\left|\frac{d^2Y}{dX^2}\right|}. \tag{10}$$

It can be deducted from Eq. (8) that:

$$\frac{d^2Y}{dX^2} = \frac{w_0}{2(1+\varepsilon_{ewx}(x))} \frac{d\left(\frac{1}{1+\varepsilon_{ewx}(x)} \frac{d\lambda_{ewy}(x)}{dx}\right)}{dx} \tag{11}$$

with the functions $\varepsilon_{ewx}(x)$, $\lambda_{ewy}(x)$ given in Section 3.2, the curvature radius r can be easily obtained with Eq. (11).

The curvature radius and the corresponding true strain for several tension stages at the minimum sections of specimen PC/ABS4-2 are shown in Fig. 9.

Similar calculation can be done for the thickness surface.

As an example, Fig. 10(a) shows the typical half width contraction ratios ($\lambda_{ewy}/2 = (w_x/w_{0x})/2$) along the axial position of specimen PC4-3 of PC. Fig. 10 (b–e) shows the specimen necking profiles at different stages corresponding to four curves of contraction ratio with the axial position in Fig. 10 (a). The curvature radius and the corresponding true strain for several tension stages at the minimum sections of specimen PC4-3 are given with the same method.

It is shown that the curvature radius decreases at first and increases with the tensile strains when it reaches its minimum at certain tensile strain. The necking speed is much higher for PC specimen than that for PC/ABS specimen. The minimum curvature radius is smaller for PC than that for PC/ABS.

3.4. Volume deformation

It is well known that dilatational deformation is an important phenomenon for polymers. G'Sell et al. [17] and Parsons et al. [19]

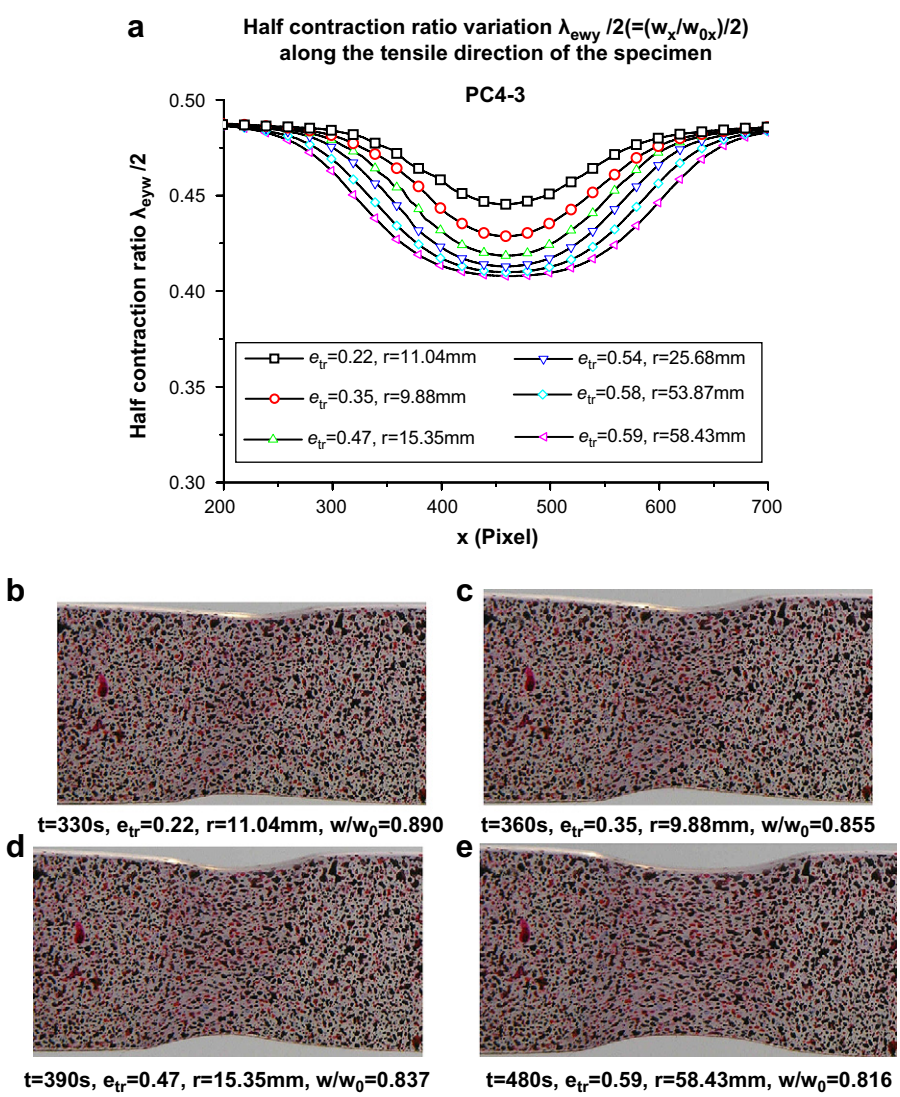

Fig. 10. Necking process and corresponding curvature radius at the minimum sections for specimen PC4-3.Here, t is the time of loading; e_{tr} and r the true strain and the curvature radius at the minimum sections. w_x/w_0x is the ratio of temporary width to the initial width at the same x position. w/w_0 is the minimum section contraction ratio of the specimen in the width direction.

have measured the volume variations of different polymers through different methods. G'Sell et al. [17] gave the volume deformation ratio by the summation of three components of strains, in which they took the two lateral strains as same by assuming the strain tensor transversally isotropic. Parsons et al. [19] gave the volume deformation ratio in term of volume strain with a similar way. However, because only the surface strains of specimens can be measured, it is difficult to give the volume deformation ratios accurately. In this study, two different methods will be used to calculate the local volume deformation ratio, in order to give a more reasonable result. One is calculated with the following formula:

$$\frac{V}{V_0} = (1+\varepsilon_e)\left(\frac{w}{w_0}\right)\left(\frac{t}{t_0}\right) = (1+\varepsilon_e)(1+\varepsilon_{eywm})(1+\varepsilon_{eytm}). \tag{12}$$

In obtaining this formula, it is assumed that the minimum specimen sections remain rectangular during the whole tensile deformation process. As shown in Figs. 6(a) and 7(a), the tensile strains at the minimum section are higher in the middle than that near the edges of the specimen during necking process. The reasons of this phenomenon can be found in Fig. 4(b). In the middle part, the deformation is concentrated in a smaller distance than that near the edges. The lateral contraction strains here are also inhomogeneous, as shown in Figs. 6(b) and 7(b). The specimen contracts more near the edges of the specimen due to the less constraint. In the stable necking region sn as shown in Fig. 5(b), the minimum section can be recognized as rectangular section reasonably, and therefore, the Eq. (12) gives a reasonable volume deformation ratio in the stable tensile stages. Fig. 11(a) and (b) shows the volume ratio variation calculated with Eq. (12) for PC/ABS and PC, respectively. It is seen that the ratio V/V_0 increases with the increase of true axial strain for PC/ABS, which is in agreement with Ref. [16,19], and then decreases with the increasing of the true axial strain. For PC, a little contraction of the volume has been measured in relatively small true strain region. It is noted from Fig. 10(b) that there are some shear deformations occurred in these stages. Because the minimum section does not keep being rectangle in these stages, therefore, the volume deformation ratio obtained this way may yield some errors here. After then, it is noted that volume deformation ratio increases rapidly to a higher value, and then decreases gradually with the increase of the true tensile strain of specimens. It is also seen that the necking speed is higher for PC than that for PC/ABS. It is observed that the scattered bands of the volume deformation ratio are larger within the true strain range from 0.15 to 0.35. This is because higher strain rate occurred in this region, and only few data points are collected within the strain range.

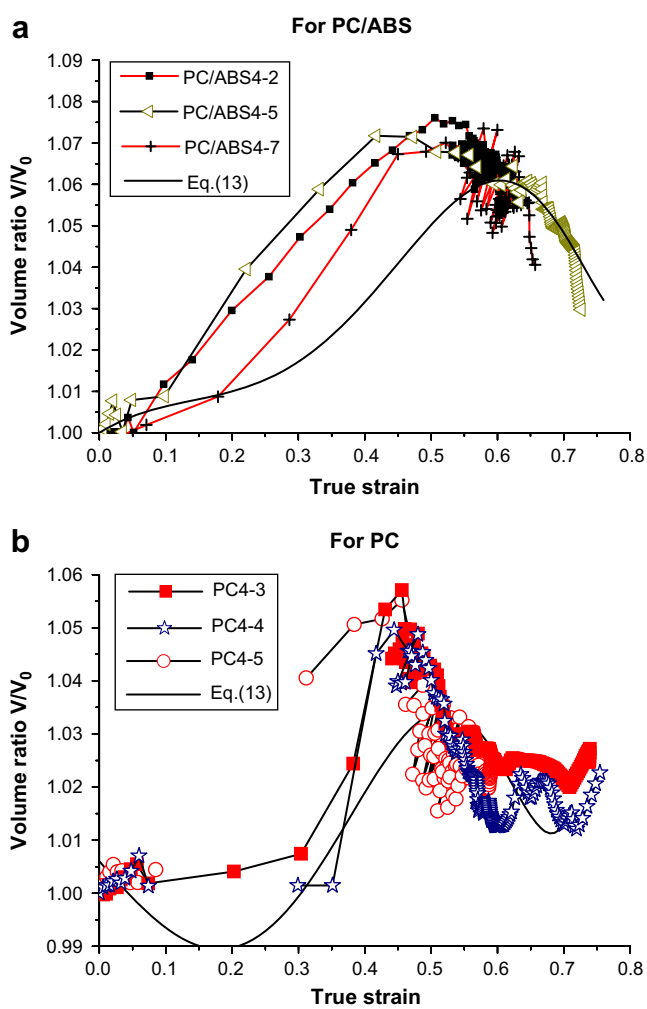

Fig. 11. Local volume variation at the minimum section of specimens during tensile deformation.

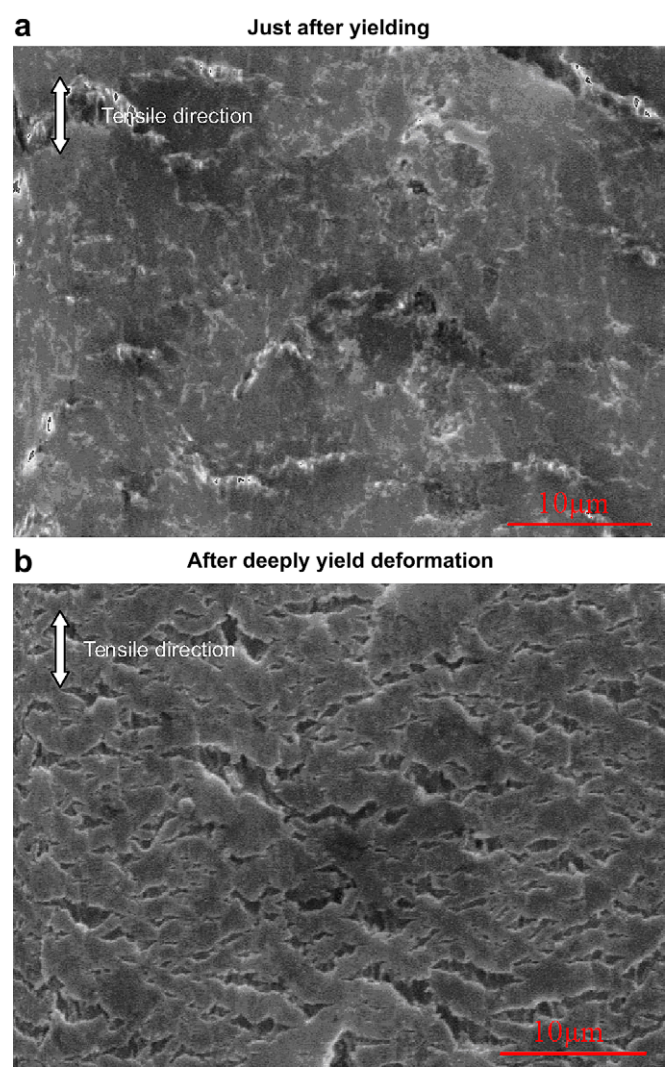

Fig. 12. Surface features of specimen after yielding deformation.

If we assume the tensile strains at the minimum section of the necking region being homogeneous, the volume deformation can be obtained with the data given in Fig. 8 (a) and (b) for PC/ABS and PC, respectively, by using the following formula:

$$\frac{V}{V_0} = (1+\varepsilon_e)^3[(w/w_0)/\lambda_w]|_{\varepsilon_e}[(t/t_0)/\lambda_t]|_{\varepsilon_e} = \exp(3e_{\mathrm{tr}})[(w/w_0)/\lambda_w]|_{(\exp(e_{\mathrm{tr}})-1)}[(t/t_0)/\lambda_t]|_{(\exp(e_{\mathrm{tr}})-1)}. \quad (13)$$

The values of $[(w/w_0)/\lambda_w]|_{\varepsilon_e}$ and $[(t/t_0)/\lambda_t]|_{\varepsilon_e}$ are the corresponding ratios at fixed engineering tensile strains ε_e. They are given from the corresponding fitting lines obtained with test data from all specimens tested for each material. Same maximum tensile strains at the two surfaces (width and thickness) at all tensile stages are assumed in this calculation. Although this is not true during necking process, but the volume ratios calculated with Eq. (13) give a reasonable tendency of local volume deformation during tensile deformation. The lines in Fig. 11 (a) and (b) show the volume ratios calculated with Eq. (13) for polymer PC/ABS and PC, respectively. It is noted that there are some differences of the volume ratios calculated with Eqs. (12) and (13). But they do give same tendency for PC/ABS and PC. The differences are due to the different assumptions given above. For PC/ABS, volume increases to a maximum value with tensile strains, and then decreases gradually. For PC, volume nearly keeps as a constant or contracts a little at smaller tensile strains, and then increases rapidly to a maximum value, after that, decreases gradually. The volume tends to increase again when the true tensile strains nearly reaches to the fracture strain. Comparing Figs. 9–11, it is found that volume increases during necking process when the curvature radius decreases with the tensile true strains, the volume increases to its maximum after the curvature radius reaches the minimum value. As we know, the stress triaxiality increases with the decreasing of the curvature radius and the contraction ratio at the minimum section in the necking region. Because the contraction ratio still decreases rapidly at the minimum curvature radius, the triaxiality of the stresses increases continually after the curvature radius reaches its minimum. It is expected that the local volume will reach its maximum when the triaxiality reaches its maximum at certain combination of curvature radius and contraction ratio. It is also observed from Fig. 11 that the volume decreases during the unloading process for both materials. This means the volume increase is partly due to the elastic deformation.

It is also seen that the volume increases more significant for PC/ABS than that for PC. This is because there is some debonding between PC and second phase ABS during tensile deformation for PC/ABS. As shown in Fig. 12, crazes have been observed on the PC/ABS specimen surface. The micro crazes or cracks become larger with the increasing of tension deformation. The crazes are generally perpendicular to the tensile direction. Although some of the crazes are not perpendicular to the tensile direction, but the fibrils in the crazes are mainly parallel to the tensile direction.

As we learned from Fig. 8, the contraction ratios in width direction are higher than that in thickness in the range of tensile engineering strains from 0.4 to 0.85, which correspond to the necking region where the triaxiality is higher. Therefore, the difference may be explained with the different stress state caused by the necking process in two directions. The necking profile curvature can also be obtained for the thickness surface. It is found the constraint is less in thickness direction than that in width direction. This is one of the reasons that causes the differences of contraction properties in two directions. Of course, the possible inhomogeneous material properties caused by the manufacture process also affect the deformation properties.

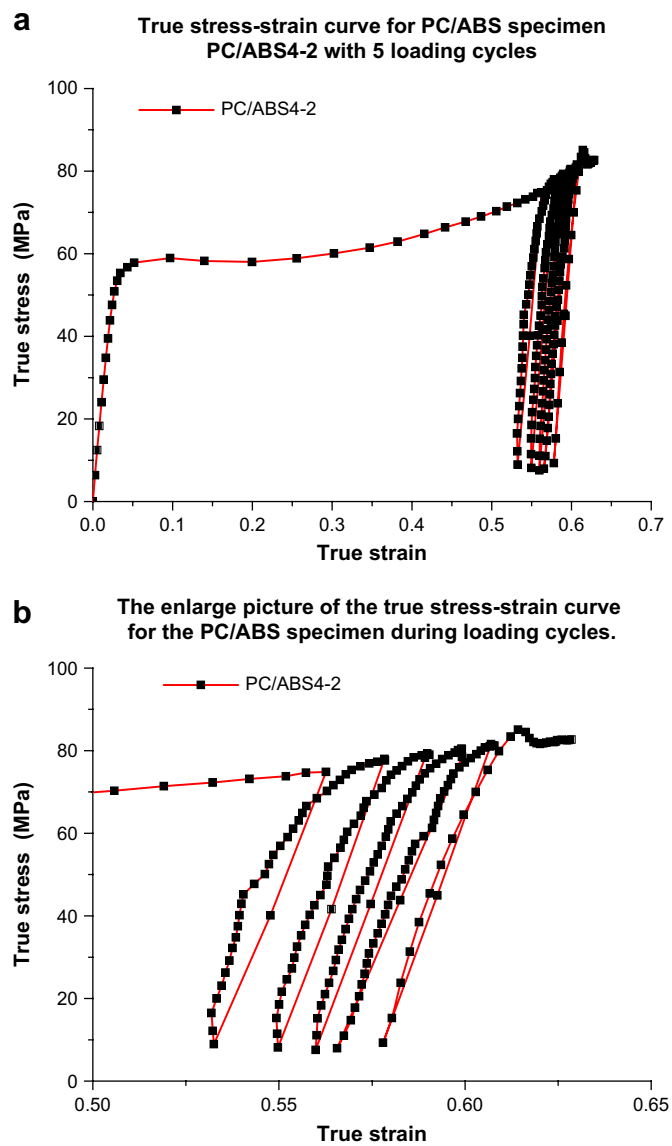

Fig. 13. The stress–strain curve for a PC/ABS specimen.

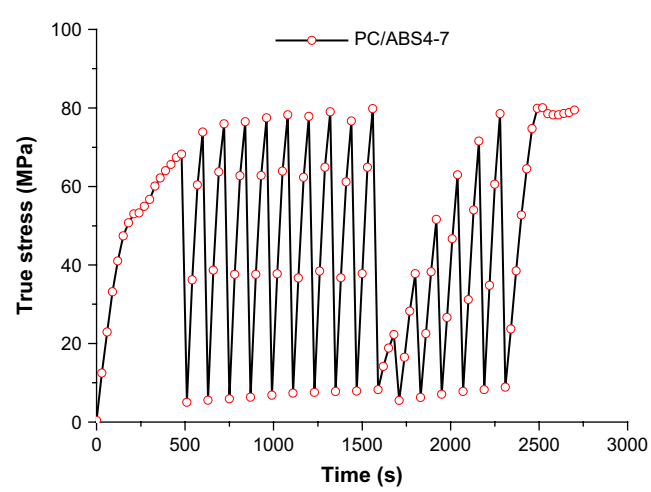

Fig. 14. True stress *vs.* time curve for specimen PC/ABS4-7.

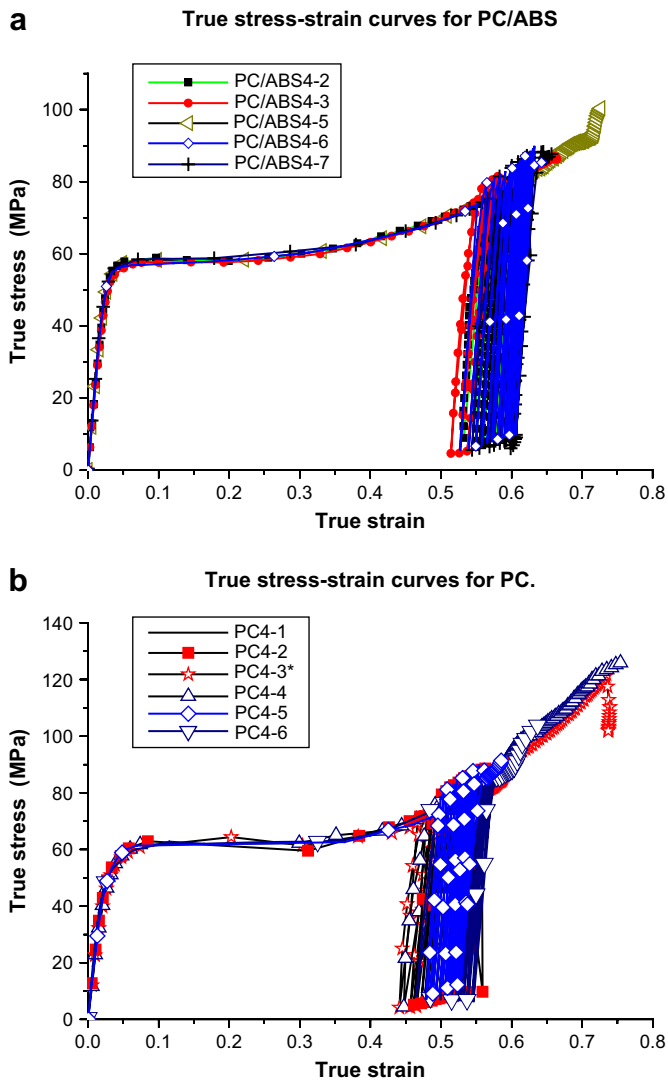

Fig. 15. True stress–strain curves for PC/ABS and PC. Note: Specimen PC4-3 has not been fractured during tension loading stage due the stroke limit of the crosshead.

3.5. True stress–strain curves

The minimum section area is calculated according the contraction ratios in width and thickness directions given by Eqs. (5) and (6) at each tensile stage.

Incorporating the initial sizes of w_0 and t_0 measured before loading and the load P, the true stress could be given with the following formula:

$$\sigma_{tr} = \frac{P}{wt} = \frac{P}{w_0 t_0} \Big/ \left(\frac{w}{w_0} \cdot \frac{t}{t_0}\right) \tag{14}$$

Fig. 13(a) shows a true stress–strain curve for one of the specimens (PC/ABS4-2) tested with a five cycling loading cycles. Fig. 13(b) shows the enlarged part of the true stress–strain curve during cycling loading process. It is observed that the area included in the hysteresis curve decreases with the increasing of the number of the loading cycles. This means that some damage occurs during the cycling loading cycles. Fig. 14 shows the true stress–time curve for one of the PC/ABS specimens tested with 15 cyclic loading cycles. It is observed that a sudden drop of test load takes place during the cyclic loading process. That means some polymer chains break in these stages. Therefore, in the next several cyclic loading processes, the true stresses are lower than the normal level due to the loading technique (displacement control). The breaking of molecular chains or sliding of entangles may cause the collapse. These need to be verified by micro mechanism observations in further investigation. Although micro mechanism observations have not been done yet, it can be concluded from the above results that cyclic loading reduces the fracture strain and fracture stress a great deal.

Fig. 15 shows the true stress–strain curves for PC/ABS and PC. Each curve is corresponding to different specimen and loading condition, denoted by different symbols in the figure. Fig. 15(a) shows the true stress–strain curves for PC/ABS, and Fig. 15(b) shows the true stress–strain curves for polymer PC. Unlike the true stress–strain curves given in [19], the true stress–strain curves for PC given in this study have no obvious stress softening occurred just after yielding. This may due to the consideration of the deformation of the two lateral directions here. As shown in Fig. 8, there are significant differences between the contraction ratios in two lateral directions. Some errors may be introduced to the results of stress–strain curves, if taking the two lateral deformations as homogenous deformation. It is also seen that both yield stress and fracture stress of PC are higher than that of PC/ABS.

It is observed from Fig. 15 that the true stress–strain curves are nearly identical each other before cyclic load being applied to each specimen for each material. After cyclic loading, both fracture stress and fracture strain decrease greatly for PC/ABS and PC. Table 1 gives the summation of the tension properties with or without cyclic loading. The reason may be some of the molecular chains break during the cyclic loading process. It is found that the fracture strains decrease rapidly with the application of the loading cycles until five cycles. Then the speed of the degradation of fracture strains and stresses slows down. However, as shown in Fig. 14, there is some collapse occurred within the subsequent loading cycles. It is

Table 1
Cyclic loading effect on the tension properties of PC and PC/ABS

Specimen	Material	Loading	Yield stress σ_y (MPa)	Fracture stress σ_f (MPa)	Fracture strain ε_f
PC4-1	PC polymer	Tension	60.21	136.9	0.7560
PC4-4		1 Cycle	61.72	125.90	0.7543
PC4-3[a]		3 Cycles	61.37	>101.77	>0.7371
PC4-2		5 Cycles	59.55	90.45	0.5959
PC4-5		15 Cycles	61.37	91.30	0.5848
PC4-6		15 Cycles	61.57	102.00	0.6089
PC/ABS4-5	PC/ABS polymer	Tension	57.77	107.38	0.7362
PC/ABS4-3		3 Cycles	57.6	86.16	0.6643
PC/ABS4-2		5 Cycles	58.0	82.72	0.6286
PC/ABS4-6		15 Cycles	57.7	85.42	0.6136
PC/ABS4-7		15 Cycles	58.4	86.67	0.6110

[a] Specimen PC4-3 has not been fractured during tension loading stage due the stroke limit of the crosshead.

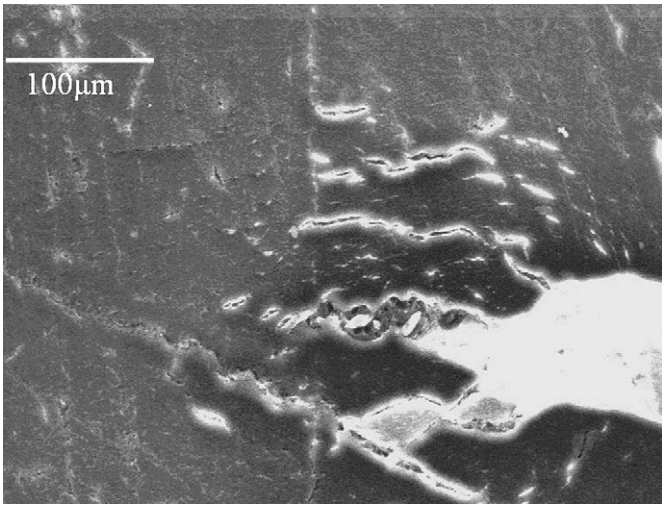

Fig. 16. Microstructure near a fatigue tip.

observed from Fig. 15 that the fracture of these specimens occurs shortly after the end of the loading cycles. In this study, the loading stress ranges span from the maximum value to a lower value. Therefore, the specimen can only bear fewer cycles before collapse occurs. If a smaller stress range is applied, the specimen may bear more cycles before collapse occurs. Li et al. [5] showed in their study that previous fatigue loading (with maximum loads being less than the yield stress of PC) led to overall embrittlement of the polymer, and detected some nanometer-sized voids or proto-crazes in the fatigue loaded specimens.

The results can be used to explain the fatigue crack growth behaviors in the future, if the constraint at crack tip is taken into consideration. As we learned from a previous study [22,23], the microstructures near a fatigue crack tip are similar to the microstructures shown in Fig. 12. Fig. 16 shows one of the pictures obtained in that study. Similar structures were also observed in literature [1,2]. It is seen from Table 1 that the degradation of the tension properties for PC is about 30% for fracture stress and 22% for fracture strain, which are larger than that for PC/ABS (about 22% for fracture stress and 16% for fracture strain). These can be used to explain the phenomenon of two times higher fatigue crack growth rates of PC than that of PC/ABS observed in [23]. This means that the above cyclic loading technique can be used to simulate the degradation of the local polymer material near a fatigue crack tip qualitatively. Further studies should be done to give a quantitatively simulation of the fatigue properties by the cyclic tension loading technique.

4. Conclusions

The DIC method and the associated data reduction schemes used in the study prove to be suitable for the measurement of the large-strain behavior of inhomogeneous deformation.

Thickness contracts more than width in the later tensile stages, and the lateral contraction ratios in width direction or in thickness direction each follow the same trend for different specimens. The curvature radius of the necking profiles at minimum section decreases at first and increases with the tensile strains when it reaches its minimum at certain tensile strain. The necking speed is much higher for PC specimen than that for PC/ABS specimen. The minimum curvature radius is smaller for PC than that for PC/ABS.

For PC/ABS, the local volume ratio increases to a maximum value with tensile strains, and then decreases gradually. For PC, the local volume ratio nearly keeps as a constant or decreases a little at smaller tensile strains, and then increases rapidly to a maximum value, after that, decreases gradually.

Cyclic loading greatly reduces the fracture stress and fracture strain for PC and PC/ABS, which correspond to the lower fatigue crack propagation resistance behaviors of PC than that of PC/ABS. For the static tensile test, PC has higher yield stress, fracture stress and longer yielding stage than PC/ABS.

Acknowledgements

This work was supported by the National Natural Science Foundation of China (10472087).

References

[1] Hu Y, Summers J, Hiltner A, Bear E. Correlation of fatigue and creep crack growth in poly (vinyl chloride). Journal of Materials Science 2003;38:633.
[2] Ishiyama C, Asai T, Kobayashi M, Shimojo M, Higo Y. Fatigue crack propagation mechanisms in poly(methylmethacrylate) by in situ observation with a scanning laser microscope. Journal of Polymer Science: Part B: Polymer Physics 2001;39:3103.
[3] O'Connel PA, Bonner MJ, Duchektt RA, Ward IM. The relationship between slow crack propagation and tensile creep behaviour in polyethylene. Polymer 1995;36:2355.
[4] Bai SL, Wang M. Plastic damage mechanisms of polypropylene/polyamide 6/polyethelene–octene elastomer blends under cyclic tension. Polymer 2003;44:6537.
[5] Li XW, Hristov HA, Yee AF, Gidley DW. Influence of cyclic fatigue on the mechanical properties of amorphous polycarbonate. Polymer 1995;36(4):759.
[6] Wang TJ, Kishimoto K, Notomi M. Effect of triaxial stress constraint on the deformation and fracture of polymers. Acta Mechanica Sinica 2002;18(5):480.
[7] Wang TJ, Kishimoto K, Notomi M. A micromechanics criterion for the ductile fracture of a polycarbonate. Key Engineering Materials 2000;183/187:121.
[8] Ramaswamy S, Lesser AJ. Microscopic damage and macroscopic yield in acrylonitrile–butadiene–styrene (ABS) resins tested under multi-axial stress states. Polymer 2002;43:3743.
[9] Manning SC, Moore RB. Reactive compatibilization of polypropylene and polymide-6,6 with carboxylated and maleated polypropylene. Polymer Engineering & Science 1999;39:1921.
[10] Buisson G, Ravi-Chandar K. On the constitutive behaviour of polycarbonate under large deformation. Polymer 1990;2071:31.
[11] G'Sell C, Hiver JM, Dahoun A, Souahi A. Video-controlled tensile testing of polymers and metals beyond the necking point. Journal of Materials Science 1992;27:5031.
[12] Nazarenko S, Bensason S, Hiltner A, Baer E. The effect of temperature and pressure on necking of polycarbonate. Polymer 1994;35:3883.
[13] Meyer RW, Pruitt LA. The effect of cyclic true strain on the morphology, structure, and relaxation behavior of ultra high molecular weight polyethylene. Polymer 2001;42:5293.
[14] Kurtz SM, Pruitt L, Jewett CW, Crawford DJ, Crane RP, Edidin AA. The yielding, plastic flow, and fracture behavior of ultra-high molecular weight polyethylene used in total joint replacements. Biomaterials 1998;19:1989.
[15] Haynes AR, Coates PD. Semi-automated image analysis of the true tensile drawing behaviour of polymers to large strains. Journal of Materials Science 1996;31:1843.
[16] Gloaguen JM, Lefebvre JM. Plastic deformation behaviour of thermoplastic/clay nanocomposites. Polymer 2001;42:5841.
[17] G'Sell C, Hiver JM, Dahoun A. Experimental characterization of deformation damage in solid polymers under tension, and its interrelation with necking. International Journal of Solids and Structures 2002;39:3857.
[18] Laraba-Abbes F, Ienny P, Piques R. A new 'tailor-made' methodology for the mechanical behaviour analysis of rubber-like materials: I. Kinematics measurements using a digital speckle extensometry. Polymer 2003;44:3883.
[19] Parsons F, Boyce MC, Parks DM. An experimental investigation of the large-strain tensile behavior of neat and rubber-toughened polycarbonate. Polymer 2004;45:2665.
[20] Fang QZ, Wang TJ, Li HM. Large tensile deformation behavior of PC/ABS alloy. Polymer 2006;47:5174.
[21] G'Sell C, Lucero AM, Gilormini P, Jonas JJ. Flow localization and the determination of constitutive relations in highly drawn polymers: one-dimensional Eulerian formulation of the effect of stress triaxiality. Acta Metallurgica 1985;33(5):759.
[22] Fang QZ, Wang TJ, Li HM. 'Tail' phenomenon and fatigue crack propagation of PC/ABS alloy. Polymer Degradation and Stability 2008;93:281.
[23] Fang QZ, Wang TJ, Li HM. Fatigue crack growth behavior of PC and PC/ABS. Acta Polymerica Sinica 2007;8:713.